Alloy Corrosion Considerations in Low-Cost, Clean Biomass Cookstoves for the Developing World ☆

Michael P. Brady [a,*], Kelly Banta [b], John Mizia [b], Nathan Lorenz [c], Donovan N. Leonard [a], Yukinori Yamamoto [a], Morgan DeFoort [b], James R. Keiser [a]

[a] Oak Ridge National Laboratory, Oak Ridge, TN 37831-6156, USA
[b] Engines and Energy Conversion Lab, Department of Mechanical Engineering, Colorado State University, 430 N. College Ave. Fort Collins, CO 80524, USA
[c] Envirofit International, Inc., 109 North College Avenue, Suite 200, Fort Collins, CO 80524, USA

ABSTRACT

Nearly 40% of the world cooks on open fires or inefficient biomass-fueled cookstoves. The resulting smoke is a health hazard, contributing to an estimated 4 million premature deaths per year, as well as a major source of black carbon emissions. One solution is the introduction of improved, clean-burning biomass cookstoves. One of the most challenging components is the combustor, which must operate at high temperatures (often ≥600 °C) in the presence of highly corrosive species released from biomass fuel combustion, yet be sufficiently low cost to permit widespread adoption. The present work reports the development of accelerated corrosion test screening protocols employing highly corrosive salt and water vapor species, specifically designed to evaluate alloys for clean biomass cookstove combustors, and corrosion findings for a range of commercial and developmental alloys. A new Fe-Cr-Si base alloy that offers promise for improved corrosion resistance at lower cost than state-of the art FeCrAl and stainless steel alloys is also reported.

© 2016 The Authors. Published by Elsevier Inc. on behalf of International Energy Initiative. This is an open access article under the CC BY-NC-ND license (http://creativecommons.org/licenses/by-nc-nd/4.0/).

Introduction

Approximately 3 billion people worldwide cook their food over open fires or basic, inefficient biomass burning cookstoves, releasing toxic emissions that cause an estimated ~4 million premature deaths a year (World Health Organization Fact sheet N°292 Household air pollution and health, 2016; Lacey and Henze, 2015; Grieshop et al., 2011; Roden et al., 2006; Smith et al., 2000; Ezzati and Kammen, 2002; Zhang et al., 2000; Venkataraman et al., 2010; Wilkinson et al., 2009). Such emissions also account for approximately 20% of the world's black carbon, with significant regional and global climate change implications (World Health Organization Fact sheet N°292 Household air pollution and health, 2016; Lacey and Henze, 2015; Roden et al., 2006). Inefficient cooking methods also result in the frequent need for time-consuming

gathering of biomass fuel, particularly by women and children, which takes time away from activities such as education or income generation, and in some circumstances represents a safety risk (World Health Organization Fact sheet N°292 Household air pollution and health, 2016). Low-cost, highly efficient improved cookstoves with increased efficiencies/reduced emissions are of interest as one approach to help solve this complex problem (Venkataraman et al., 2010; Kshirsagar and Kalamkar, 2014; Kumar et al., 2013; Sutar et al., 2015; Still et al., 2015; L'Orange et al., 2012; Tryner et al., 2014; Urmee and Gyamfi, 2014).

Significant recent progress has been made for improved cookstove design, combustion modeling, and emissions reductions (Kshirsagar and Kalamkar, 2014; Kumar et al., 2013; Sutar et al., 2015; Still et al., 2015; L'Orange et al., 2012; Tryner et al., 2014; Urmee and Gyamfi, 2014; MacCarty and Bryden, 2015). The success of clean biomass cookstoves from an engineering standpoint is, however; also critically dependent on the materials of construction. One of the most challenging components is the combustor, which operates at high temperatures (often ≥600 °C) in the presence of highly corrosive species (water vapor, chlorine, sulfur, salts, ash, and deposits) derived from the combustion of biomass fuels (Antunes and de Oliveira, 2013; Saidur et al., 2011). Such conditions pose a significant challenge, since materials must be low-cost in order to permit widespread adoption in the developing world, but must also be corrosion resistant and durable. Metallic alloys offer the best combination of ease of manufacturing, low mass,

robustness/mechanical integrity, and design flexibility, but are also far more susceptible to corrosion than ceramic combustion chambers. In particular, mixed oxidant and ash/salt deposit-induced, biomass-related high-temperature corrosion (Antunes and de Oliveira, 2013) can result in order of magnitude and higher increases in alloy corrosion rates (depending on alloy composition, temperature, and environment) compared to air oxidation.

Corrosion of alloys under biomass combustion conditions has been an active area of research in recent years for industrial scale power generation applications (e.g. power plants, boilers, etc.) that use biomass as a renewable alternative to fossil fuels (Antunes and de Oliveira, 2013; Baxter et al., 1998; Saidur et al., 2011; Okoro et al., 2015). Laboratory corrosion test exposure standards and protocols are available, particularly with regards to introduction of ash/salt deposits and their interactions with flue gas (combustion exhaust products containing SO_x, Cl, etc. species) [e.g. 21] There is some qualitative overlap for biomass cookstoves with regards to the corrosive species encountered, particularly salts, sulfur, and water vapor. However, the temperatures, pressures, combustion environments, biomass fuel sources, corrosive species concentrations and deposit tendencies, alloy mechanical property requirements, and component lifetimes encountered in these power generation applications can differ considerably from those of low-cost (~$10–50 range), individual cookstoves that burn local biomass fuels and have targeted lifetimes typically on the order of ~3000–5000 hot hours. In a search of the literature, we were unable to identify research efforts specifically devoted to corrosion issues in improved biomass cookstoves. The present work seeks to address this gap by pursuing studies to 1) establish accelerated corrosion screening protocols to assess candidate alloys to achieve durable improved biomass cookstoves, 2) achieve insight for the relative corrosion behavior of stainless steels and related heat-resistant alloys under cookstove-relevant conditions, and 3) identify promising alloy design approaches to low-cost alloys and coatings to enable more durable, longer-lived cookstoves.

Materials and Methods

Alloy Considerations

Resistance to high-temperature (≥ 600 °C) corrosion is achieved by the formation of continuous, protective, slow-growing oxide surface layers (scales) in service, typically based on Al_2O_3, Cr_2O_3, and/or SiO_2, and (occasionally) NiO (Brady et al., 2000). Alloys for study (Table 1, all compositions in weight percent, wt.%) were selected to survey a range of protective oxide-scale forming types and a range of base alloy compositions potentially relevant to cookstove combustors (DeFoort et al., 2014). These include ferritic alloys, based on body-centered-cubic (BCC) Fe, and austenitic alloys, based on face-centered cubic (FCC) Fe, which offer better high-temperature strength than ferritics but are also more costly due to their high Ni contents (Ni stabilizes FCC Fe) (Brady et al., 2014). Commercial alloys evaluated included ferritic, alumina-forming FeCrAlY (Fe-20Cr-5Al base) (DeFoort et al., 2014) and austenitic, chromia-forming type 310S stainless steel (Fe-25Cr-20Ni base), which are considered state-of-the-art cookstove combustor alloys for their balance of relatively low cost and good high-temperature corrosion resistance. Lower-cost commercial austenitic type 316 L (Fe-17Cr-10Ni base), austenitic type 201 (Fe-18Cr-7Mn-5Ni base) and ferritic type 446 (Fe-25Cr base) stainless steels were also evaluated. Materials such as mild or galvanized steels were not evaluated as they are not suitable for the ≥600 °C temperatures encountered in the combustion chamber of improved biomass cookstove designs, and rapidly corrode at these temperatures.

Developmental model alloys based on ferritic Fe-15Cr with 3Si, Fe-15Cr with 5Al and 3Si, and Fe-25Cr-5Al were studied to further assess the relative effects of Al, Cr, and Si additions. Three developmental alumina-forming austenitic (AFA) alloys were also studied, employing levels of Ni additions at 25Ni, 20Ni, and 12Ni wt.% (Ni levels are a key cost driver for stainless steel alloys) (Brady et al., 2014). Unalloyed Ni (referred to as "pure" Ni for simplicity) was studied as a surrogate for a Ni-cladding as well as for insights into the corrosion mechanism. Pre-oxidized FeCrAlY (1100 °C for 2 h in air, which yielded specific mass gains of 0.5–0.6 mg/cm^2) with a ~ 1–3 μm alumina surface layer pre-formed prior to testing was also studied, both for mechanistic insights and as a potential route to improved corrosion resistance.

Alloy Corrosion Test Sample Preparation

Commercial 316 L, 310S, and FeCrAlY alloys were procured in sheet form, 446 in round bar form, and the pure Ni and 201 in plate form (Table 1). The three developmental AFA alloys (Table 1) were obtained in solutionized plate form from hot-rolled and machined ~15 kg vacuum induction melted ingots (alloy process details are provided in reference Brady et al. (2014)). The model FeCrAlSi, FeCrSi, and Fe25CrAl

Table 1
Analyzed compositions in wt.% of developmental and commercial alloys by inductively coupled plasma and combustion techniques. (Impurities ≤ ~0.05 wt.% not reported).

	Fe	Ni	Cr	Al	Si	Mo	Mn	Ti	C	other
FeCrAlSi	75.99		14.56	5	2.81		0.47	0.49	0.066	
FeCrSi	80.85		15.15		2.44		0.47	0.47	0.57	
Fe25CrAl	68.99		25.1	4.84	0.01			0.47	0.07	
FeCrAlY	73.04	0.12	20.42	5.65	0.24		0.18		0.016	0.05Y, 0.04Hf 0.05Zr
310S	53.23	18.83	25.17		0.59	0.43	0.91		0.03	0.3Cu 0.17Co 0.09 V 0.06Nb
446	74.1	0.17	24.09		0.26		0.75		0.058	0.14 V 0.11Nb
316 L	67.86	9.98	17.08		0.43	2.1	1.56		0.026	0.46Cu 0.07 V
201	70.73	4.42	16.21		0.5	0.26	6.79		0.085	0.71Cu 0.07Co 0.068 N
AFA-25Ni	51.83	25.04	13.84	3.56	0.13	0.18	1.99		0.114	2.51Nb 0.51Cu 0.16 W
AFA-20Ni	57.61	19.96	13.87	3.06	0.12	1.99	1.99		0.152	0.6Nb 0.52Cu
AFA-12Ni	62.39	12.02	13.91	2.52	0.11	0.11	4.97		0.201	3.06Cu 0.59Nb
Pure Ni	0.09	99.44			0.04		0.23		0.068	0.06Co

alloys (Table 1) were vacuum arc cast in small, laboratory scale 2.5 cm × 2.5 cm × 10 cm ingots, solutionized at 1200 °C for 1 h in Ar-4H$_2$ gas, and then hot rolled at 1100 °C to 50% reduction using 5–10% reduction per rolling pass. Test samples 20 × 10 mm × 0.75 to 1.2 mm for lab furnace evaluation and 2.5 cm × 12.5 cm × 0.75 to 1.2 mm with a 4 mm diameter hole for in-situ cookstove evaluation were electro-discharged machine (EDM) cut. For the thin sheet 316 L, 310S, and FeCrAlY samples, the as-processed surface finish was retained for corrosion testing. For all of the other alloy product forms, the EDM-cut surface finish of the test sample faces was polished to 600 grit finish by standard metallographic techniques in water using SiC grinding papers.

Corrosion Testing

Corrosion evaluation under cookstove-relevant conditions was studied by two methods: 1) lab furnace testing and 2) in-situ exposure in an operating cookstove. The lab furnace testing was conducted in air with 10 volume percent (vol.%) H$_2$O to simulate water vapor release from burning biomass, and direct deposition of salt onto the test samples to simulate the burning of highly corrosive biomass feedstocks. In particular, relatively high levels of salt species are encountered in many types of biomass and can lead to significantly accelerated alloy corrosion rates (Antunes and de Oliveira, 2013; Baxter et al., 1998; Saidur et al., 2011; Okoro et al., 2015). The in-situ cookstove testing was conducted using wood fuel that was pre-soaked in a salt water solution to yield accelerated, highly corrosive conditions.

Test sample corrosion was evaluated by two approaches: specific mass change (balance accuracy of ~ ± 0.04 mg or 0.01 mg/cm^2), which can be measured nondestructively with the sample returned to testing for additional exposure time, and metal loss measurements, which required removal of a given sample from testing for destructive, cross-section analysis to determine the thickness of intact metal remaining after a given exposure period. During corrosion, the test sample mass increases from incorporation of oxygen into the alloy from the environment and the subsequent formation of oxides on and/or within the sample (also holds true for nitrogen, sulfur, etc. species). Volatilization and/or flaking off of the oxide, etc. corrosion products result in mass losses. In this manner the kinetics of corrosion can be followed by mass change measurements. Combined with cross-section metal loss measurements, a more complete picture of corrosion kinetics can be obtained.

Lab furnace Corrosion Testing

Electrical-resistance heated lab furnace corrosion exposures were conducted in 100 h cycles at 600 and 800 °C in air with 10 vol.% water vapor, with sample mass changes measured after every 100 h furnace cycle (air cooling of the test samples). Three replicates of each alloy were exposed, with samples sequentially removed from testing after 100, 500, and 1000 h for cross-section analysis. (The 1000 h of testing represents ~2.7 hot hours per day cookstove use for a year; although

it is important to note that the conditions employed in the present work were accelerated by the use of salt species). The water vapor was introduced by atomization of distilled water into the flowing gas stream above its condensation temperature. The tests were conducted in a ~ 8.1 cm diameter alumina tube furnace using flow rates of ~925 or 760 cm^3/min (air) and ~4–5 cm^3/h (water) at 600 and 800 °C, respectively. To introduce salt to the test samples, a 3.5 wt.% salt solution was made using distilled water and Instant Ocean® Sea Salt (Blacksburg, VA 24060–6671 USA), a product which simulates the salt species (Na, K, Mg, etc. chlorides) present in natural seawater.

The test samples were placed across alumina rods in a flat alumina tray (Fig. 1a). The top surfaces of the test samples were sprayed with salt water and allowed to air dry prior to initial exposure in the furnace, and salt water was re-applied after every 100 h cycle. (Mass change measurements for corrosion assessment were taken after every cycle prior to adding salt). The salt solution was sprayed only on the top-oriented test sample face (exposed surface), and the same top face was maintained for salting across all test cycles. (Orientation of the samples was maintained to salt the same top face across all test cycles.) Salt additions after drying were typically in the range of ~0.5 to 1.5 mg/cm^2 of salt per top-exposed sample face.

In-Situ Cookstove Testing

The in-situ cookstove evaluation was performed using two Envirofit International (Fort Collins, CO USA) B1200 ceramic lined, rocket elbow type stoves fed with salted wood. Test fixtures were created to hang samples at a fixed depth inside the combustion chamber of each stove such that they would be exposed directly to the flame region (Fig. 1b). Each fixture held up to fifteen samples at a time. In order to ensure even exposure, fixtures were rotated every hour of burn time. Test samples were removed after every 50 h of burn time, mass change registered, and returned to testing. As with the lab furnace evaluation, three replicates of each alloy were exposed, with samples sequentially removed from testing after 100, 500, and 1000 h for cross-section analysis.

The "lab wood" burned in the in-situ test was ~20 mm x by 20 mm cross-section by 305 mm length clear Pine trim. In order to produce accelerated corrosion conditions, a procedure was developed to controllably introduce salt (halogen) content into the lab wood to a level similar to that found in a biomass fuel known to cause highly corrosive conditions. Two types of Haitian charcoal that were observed to produce highly corrosive combustor conditions were analyzed for halogen content: Mangrove lump charcoal and Chabon Ticadaie briquette charcoal, with 760 μg/g and 1390 μg of halogen per g of charcoal, respectively, yielding an average value of 1075 μg/g halogen. (It should be noted that high halogen content can be encountered in a wide range of biomass around the world (Antunes and de Oliveira, 2013; Baxter et al., 1998; Saidur et al., 2011), and is not limited only to Haitian charcoal). The 1075 μg/g was used as a target value for the halogen content of the lab clear Pine wood, which was achieved by soaking the wood in a
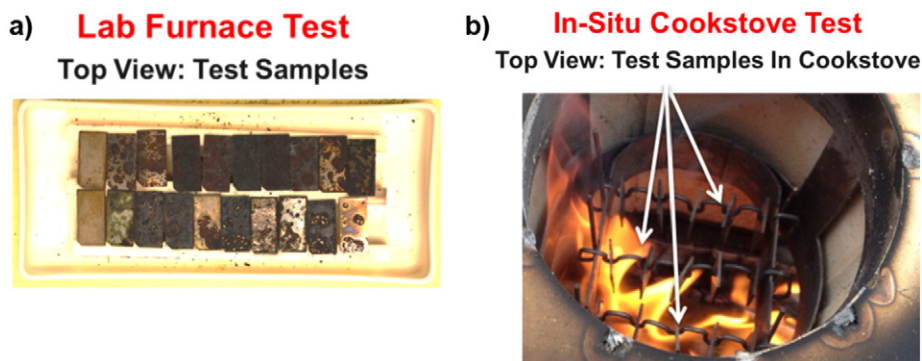

Fig. 1. Photographs of (a) lab furnace testing alumina tray with samples, and (b) in-situ cookstove testing.

tank of synthetic sea water solution for several days. Water was continuously circulated by a pump to promote even mixing of the salt. After soaking, the wood was air-dried for at least 2 days in ambient air and then dried in an oven at 104 °C for an additional 2 days before burning. Instant Ocean® Sea Salt was again used to create the salting solution. An initial target value for salt concentration in the water was determined by analyzing the halogen content of processed wood that was soaked in 1.9 l jars with different salt concentrations. Based on this initial salt concentration target value, several small batches of salted wood were produced and analyzed for halogen content. Because the halogen content of the initial salted fuel was lower than desired (Table 2), the salt quantities were increased in subsequent batches in order to more closely match the halogen content of the Haitian charcoals. A total of ten batches of wood were processed and burned in the in-situ cookstove testing. An average value of ~1070 μg of halogen per g of wood was achieved (Table 2).

Three salted clear Pine wood sticks were fed at a time into the cookstove, and sticks were kept so they were always touching to reduce variability in burn rate due to stick spacing. After every 2–3 sets of sticks burned, char and ash that had accumulated in the chamber was removed. Each day of testing, cookstoves were burned continuously for an average of ~6 h. The average fuel consumption rate was 570 g/h. To determine the range of temperatures that the alloy test samples would experience, a thermocouple was placed inside the chimney of each stove at the same height as the coupon fixture. Typical combustion chamber temperature profiles for the cookstoves, where test coupons were placed, are shown in Fig. 2. The average gas temperature range during steady state in-situ testing was 663 °C ± 85 °C. If transient operation events such as startup, shutdown, and char/ash removal are included in the chamber temperature calculations, the average exposure temperature decreases to an average of 609 °C ± 188 °C. As the majority of the testing was performed in the steady state configuration, under controlled conditions, the average exposure temperature and variability was likely closer to 663 °C ± 85 °C than the 609 °C ± 188 °C over the course of the 1000 h of testing.

Fig. 3 shows in-situ cookstove corrosion specific mass change data for the state-of-the-art FeCrAlY alloy (Table 1) when the stove was burned with as-received clear Pine wood vs. salted clear Pine wood. Parabolic-like (rate decreasing with time) corrosion kinetics with relatively low specific mass gains were observed for the FeCrAlY when as-received clear Pine wood was burned, consistent with protective oxide scale formation. In contrast, much more rapid mass gains and a period of mass loss resulting from oxide scale spallation were observed when the salted clear Pine wood was burned. The salting procedure adopted therefore clearly induced a more corrosive test environment to serve as an accelerated test method for evaluation of candidate combustor materials.

Table 2
Halogen content of lab-salted wood.

Batch #	Water (liter)	Salt (g)	Wood (kg)	Halogen Content (μg/g)
1	136.27	400	36	281
2	128.70	400	40	650
3	124.92	350	42	776
4	567.81	3675	113	700
5	624.59	5250	192	821
6	719.23	5250	199	1780
7	681.37	5250	117	548
8	662.45	5250	218	781
9	745.73	5250	175	1550
10	745.73	5250	239	1275
Weighted Average All Batches	639.73	4700	177	1070
Weighted Average* Batches 5–10	696.52	5250	198	1160
Std. Dev. Batches 5–10	49.21	0	44	485

* Soaking process was being developed during batches 1–5, and thus halogen content differed from batch to batch. The final salting process was used for batches 5–10 which accounted for 83% of the total wood used in the in-situ cookstove alloy corrosion testing.
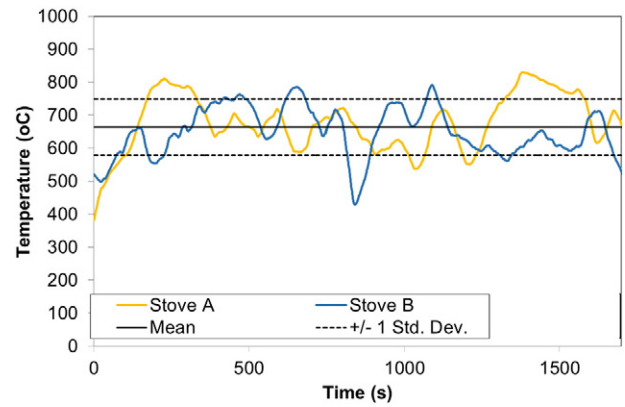

Fig. 2. Temperature profiles for the well-controlled portion of the burn cycle with 3 wood sticks for the two cookstove test beds.

Cross-Section Analysis of Corroded Samples

Exposed test samples were cross-sectioned by low-speed diamond saw and prepared by standard metallographic techniques (oil-based rather than aqueous polishing media was used to avoid dissolution of possible chloride and related corrosion products during sample preparation). The cross-sections were analyzed by light microscopy, scanning electron microscopy (SEM) with energy dispersive x-ray spectroscopy (EDS), and electron probe microanalysis (EPMA) using both EDS and wavelength dispersive spectroscopy (WDS). Initial sample thickness was measured with a micrometer. Cross-section thickness measurements of corroded samples were made using an optical measurescope (light microscope with digitized micrometer stage measurement attachment). The test sample cross-sections along the 10–12.5 mm sample width were divided into 3 regions, not including 1 mm from the sample end corners. In each of the 3 sample regions, the area of greatest corrosion attack was selected for measurement of intact metal remaining in cross-section. The boundary of the intact metal remaining was defined as the point at which the underlying metal was free of oxide scale and internal attack. The average of the three locations of greatest attack was used to plot metal loss vs. time in Figs. 4-6 (reported in the plots as ±1 standard deviation).

Results

Corrosion Data

Corrosion data from 600 °C lab furnace testing, 800 °C lab furnace testing, and in-situ cookstove testing are shown in Figs. 4-6. (Raw data are supplied in the supplemental material). All of the alloy samples in
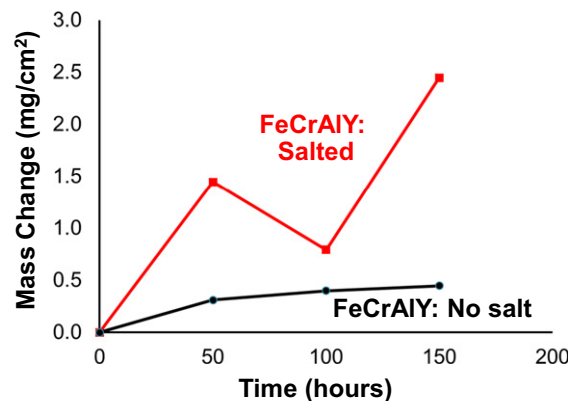

Fig. 3. Corrosion data for the commercial FeCrAlY alloy from in-situ cookstove testing using as-received clear Pine wood and salted clear Pine wood.

a) Mass Change: Commercial Alloys

b) Metal Loss: Commercial Alloys

c) Mass Change: Developmental Alloys
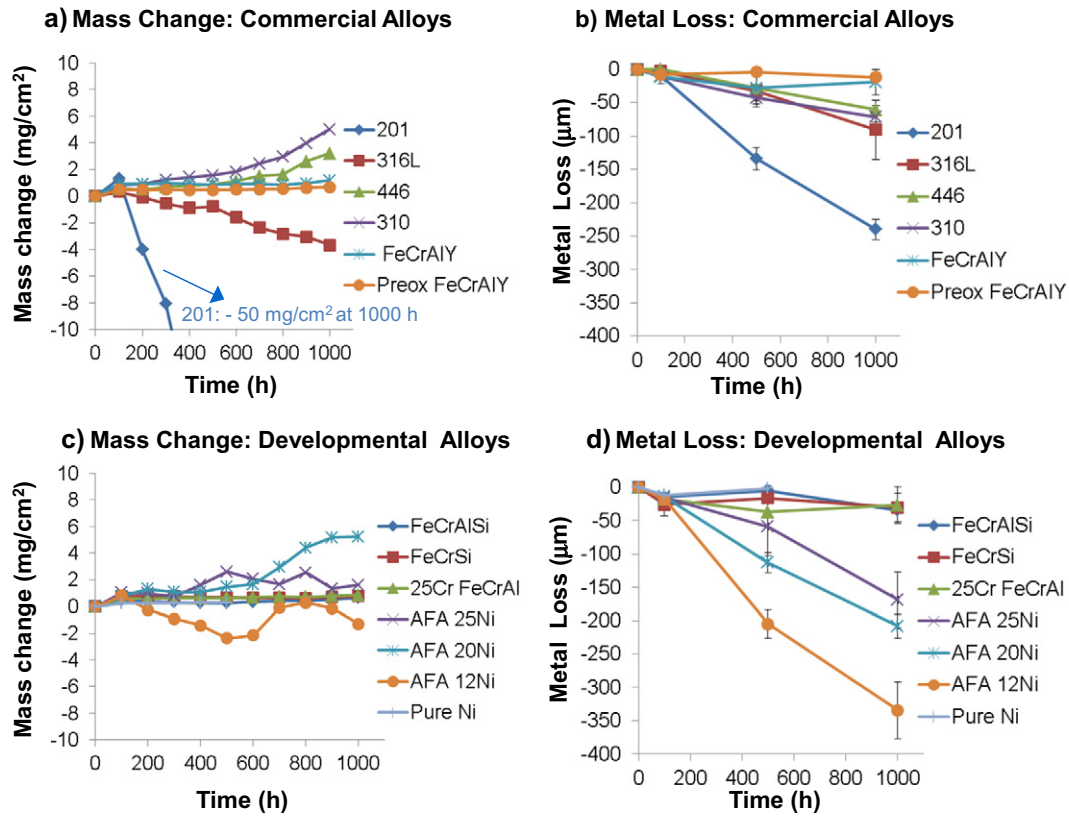
d) Metal Loss: Developmental Alloys

Fig. 4. Specific mass change (a, c) and metal loss (b, d) corrosion data from 600 °C lab furnace testing of commercial (a, b) and developmental alloys (c, d). The metal loss data is plotted as the average ± 1 standard deviation of the 3 locations of greatest attack. The environment was air + 10% H_2O, with salt added at the start of testing and re-applied after every 100 h cycle.

a) Mass Change: Commercial Alloys

b) Metal Loss: Commercial Alloys

c) Mass Change: Developmental Alloys

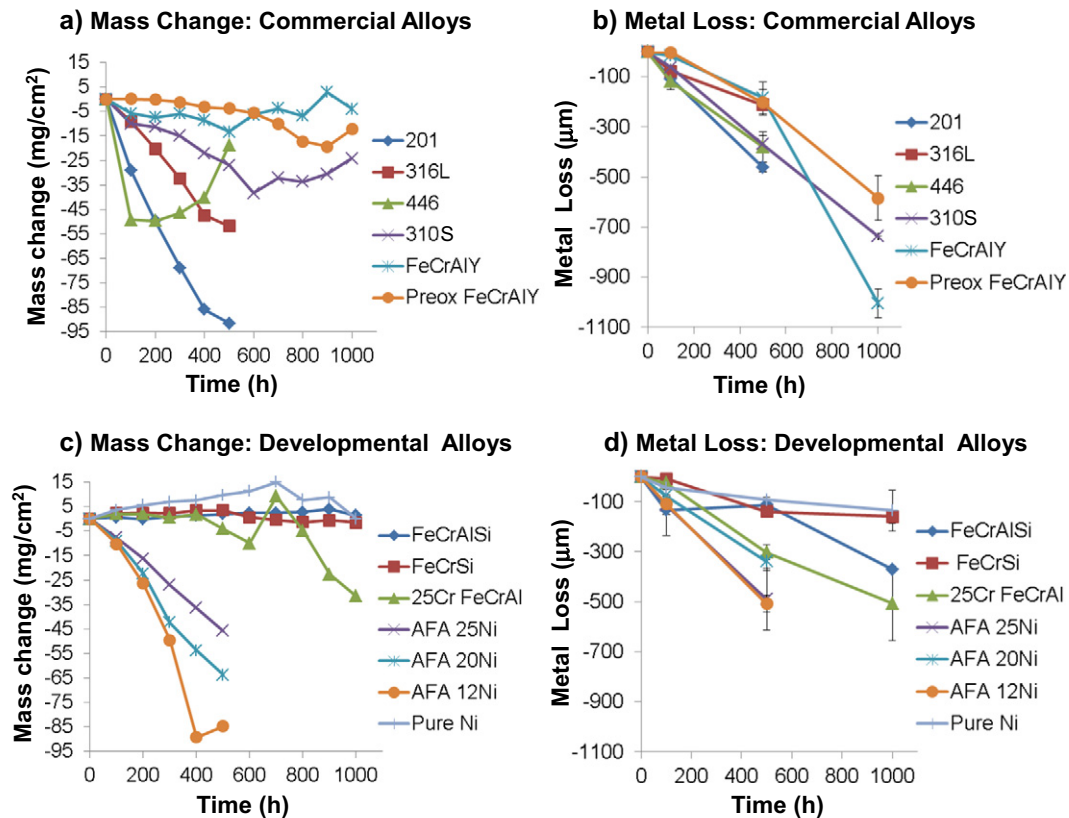**d) Metal Loss: Developmental Alloys**

Fig. 5. Specific mass change (a, c) and metal loss (b, d) corrosion data from 800 °C lab furnace testing of commercial (a, b) and developmental alloys (c, d). The metal loss data is plotted as the average ± 1 standard deviation of the 3 locations of greatest attack. The environment was air + 10% H_2O, with salt added at the start of testing and re-applied after every 100 h cycle.
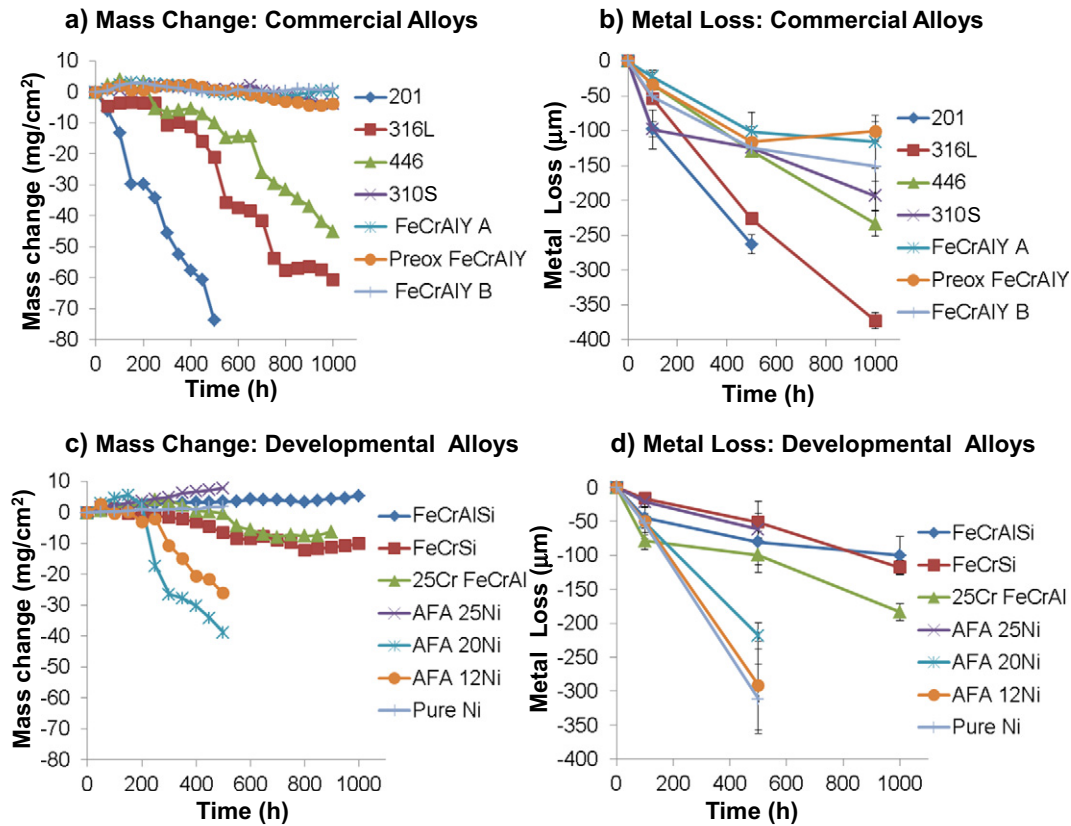
Fig. 6. Specific mass change (a, c) and metal loss (b, d) corrosion data from in-situ coookstove testing of commercial (a, b) and developmental alloys (c, d). The metal loss data is plotted as the average ± 1 standard deviation of the 3 locations of greatest attack. FeCrAlY A and FeCrAlY B are duplicate samples run in each of the two cookstove test beds utilized. Salted clear Pine wood was burned to induce accelerated corrosion conditions.
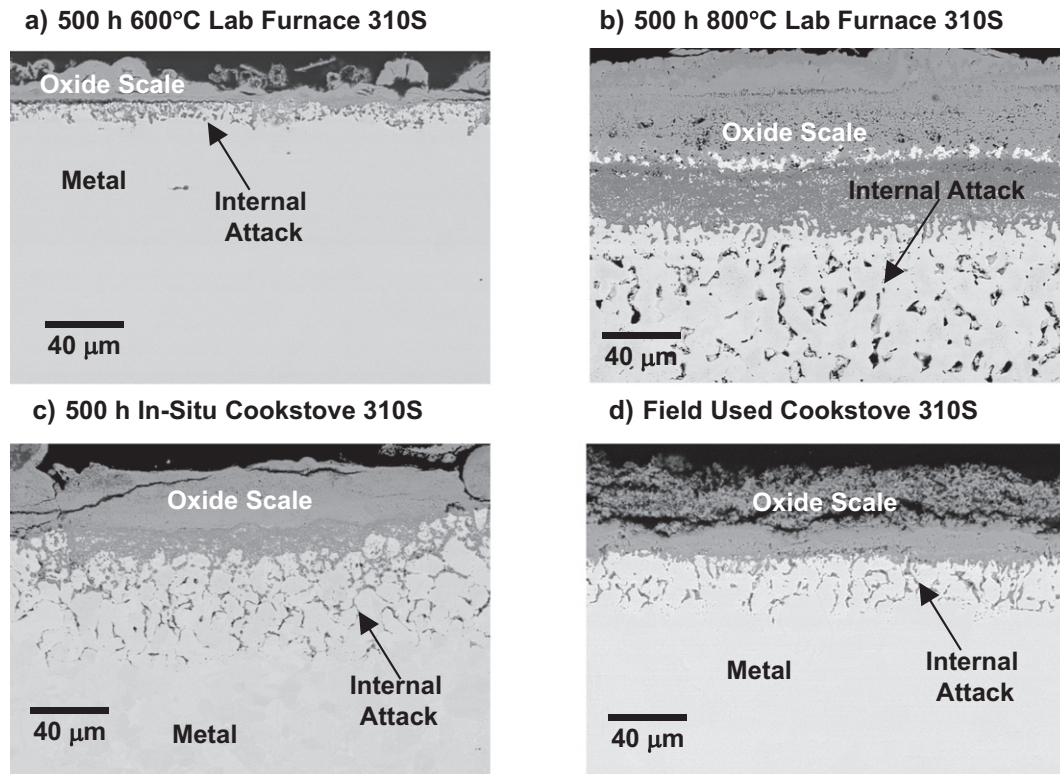

Fig. 7. Cross-section backscattered electron mode SEM images of 310S stainless steel after 500 h exposure in (a) 600 °C lab furnace testing, (b) 800 °C lab furnace testing, and (c) in-situ cookstove testing. A cross-section of a 310S combustor from a field-operated cookstove is shown in (d) for comparative purposes.

both lab furnace and in-situ cookstove testing showed loose, non-adherent oxide scales typical of Fe-oxide formation/relatively rapid corrosion developing within the first 100 h of exposure under all test conditions evaluated. In the 600 °C lab furnace testing (Fig. 4), specific mass changes were on the order of ± 5 mg/cm^2 over the course of 1000 h of total exposure (100 h cycles) for all commercial and developmental alloys, with the exception of type 201 stainless steel which exhibited extensive corrosion and specific mass loss in excess of

-50 mg/cm^2. Cross-section metal loss measurements (Fig. 4 b, d) proved far more useful in distinguishing the relative degree of alloy corrosion resistance than the specific mass change measurements. This is because a combination of mass gain from oxide scale formation and mass loss from oxide scale spallation (or volatilization) can result in low net mass changes despite appreciable corrosion. The cross-sectioning analysis also permits assessment of the extent of internal corrosion vs. external scaling.

Consistent with the specific mass change measurement of -50 mg/cm^2, the type 201 stainless steel exhibited extensive cross-sectional metal loss, ~ -240 μm after 1000 h of exposure in the 600 °C lab furnace test. However, despite relatively low specific mass changes (-1 to 5 mg/cm^2), significant cross-section metal loss was also observed for the three AFA alloys, with ~ -170 μm, -210 μm, and -330 μm metal loss for AFA-25Ni, AFA-20Ni, and AFA-12Ni, respectively. The commercial stainless steels exhibited lower corrosion rates, with metal losses of ~ -60 μm, -70 μm, and -90 μm after 1000 h for type 446, type 310S, and type 316 L, respectively.

The lowest metal losses for the Fe-base alloys in the 600 °C lab furnace test were registered for the commercial FeCrAlY, which had metal losses of ~ -30 μm after 500 h, and -20 μm after 1000 h. The 500 and 1000 h data are from different FeCrAlY test samples and are in the range expected for sample-to-sample variation and initial test sample thickness measurement scatter, estimated to be ~ $\pm$
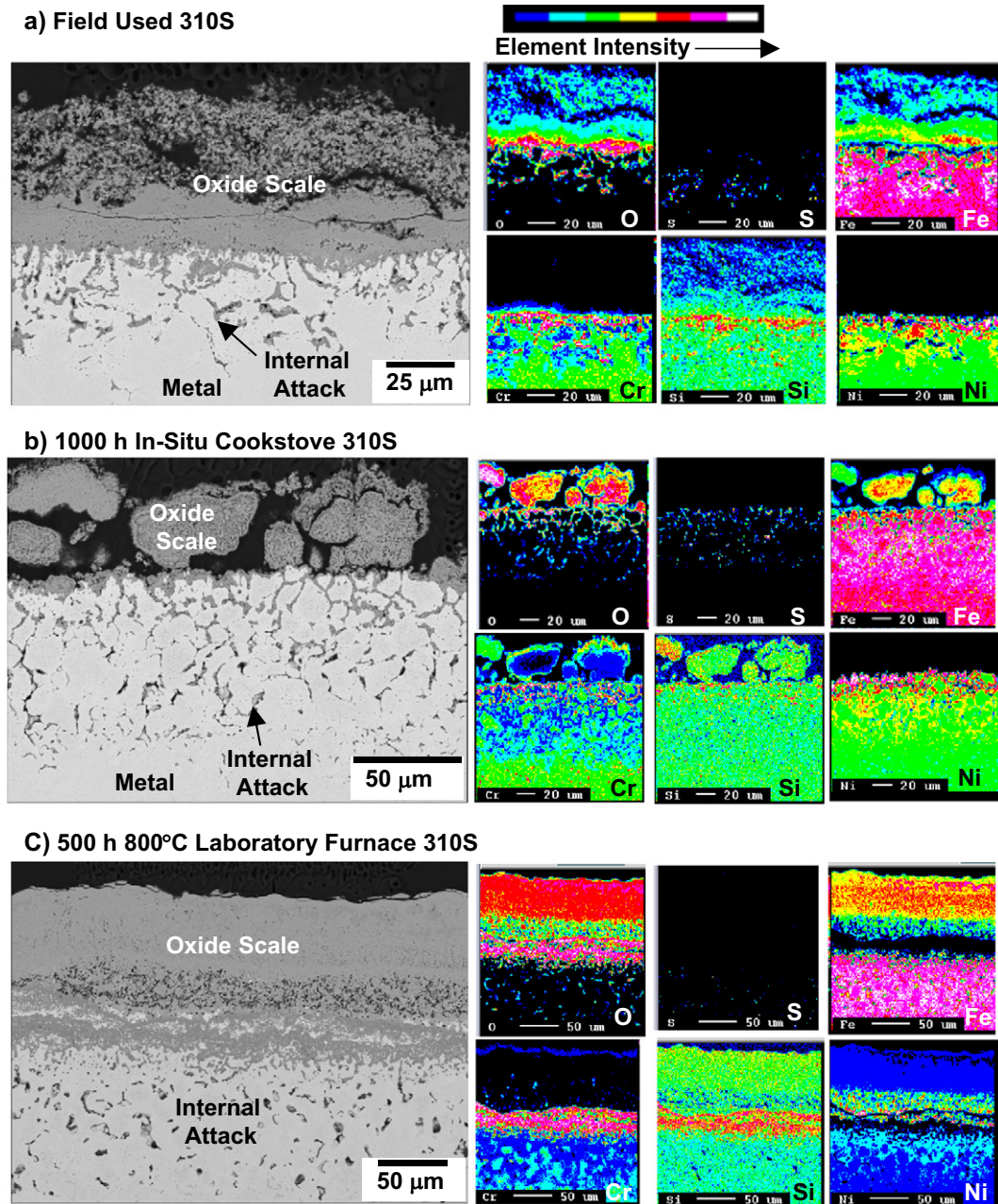

Fig. 8. Cross-section backscattered electron mode EPMA images and corresponding elemental maps for (a) a 310S field operated cookstove combustor, (b) 310S after 1000 h of in-situ cookstove testing, and (c) 310S after 500 h of 800 °C lab furnace testing.

10–20 μm. Pre-oxidation of the FeCrAlY resulted in an even lower metal loss measurement, −10 μm after 1000 h. The developmental FeCrSi, FeCrSiAl, and Fe25CrAl alloys also exhibited low metal losses, in the range of −25 to −35 μm (Fig. 4d). As a whole, these metal loss measurement values for the Fe-Cr-Al and Fe-Cr-Si alloys indicate similar, relatively good levels of corrosion resistance under these accelerated corrosion conditions. Consistent with its known good corrosion resistance to high-temperature salt species attack under some conditions (Jonsson et al., 2015; Li et al., 2005), the pure Ni showed little visible evidence of corrosion, with specific mass changes of only 0.3 mg/cm^2 (Ni tested only to 500 h total exposure at 600 °C) and metal loss of −11 μm, which is within the expected error for the cross-section metal loss corrosion assessment method.

Much faster corrosion rates were observed in the 800 °C lab furnace testing (Fig. 5), where evaluation of most alloys stopped after 500 h of exposure due to excessive corrosion (mass losses in excess of −40 to −50 mg/cm^2 and cross-section metal losses in excess of several hundred μm). Of the alloys tested to 1000 h, (FeCrAlY, pre-oxidized FeCrAlY, 310S, FeCrAlSi, FeCrSi, Fe25CrAl, and pure Ni), only the FeCrSi and pure Ni samples exhibited good corrosion resistance, with 1000 h metal losses of ~ −160 μm and ~ −135 μm, respectively. The FeCrAlY and 310S alloy samples were consumed through-thickness in some cross-section locations (starting sample thickness of ~1 mm and ~0.75 mm, respectively). The pre-oxidized FeCrAlY and the Fe25CrAl samples exhibited metal losses in excess of ~ −500 μm at 1000 h, and the FeCrAlSi sample ~ −370 μm.

Fig. 6 shows corrosion data for the in-situ cookstove testing. A comparison with Figs. 4 and 5 shows that the corrosion rates were essentially intermediate between the 600 °C and 800 °C lab furnace testing, consistent with the ~663 °C average temperature of the in-situ cookstove testing (Fig. 2). Relative alloy corrosion resistance trends were generally similar to the lab furnace testing, indicating the utility of the lab furnace protocol as a screening tool to down-select candidate alloys for the more costly and time intensive in-situ cookstove testing. Type 201 stainless steel, type 316 L stainless steel, and the 12 and 20Ni AFA alloys all exhibited relatively poor corrosion resistance in the in-situ cookstove testing, with metal losses in excess of −200 μm after only 500 h of exposure, consistent with the lab furnace trends.

The lowest corrosion rates in the in-situ cookstove testing were exhibited by the FeCrAlY, pre-oxidized FeCrAlY, FeCrAlSi, and FeCrSi alloys, with metals losses in the −100 to −150 μm range after 1000 h (Fig. 6). The types 310S and 446 stainless steels exhibited moderately worse corrosion resistance, with metal loss values of −190 μm and -230 μm after 1000 h. The two major exceptions between lab furnace and in-situ cookstove testing were the pure Ni and the 25Ni AFA alloy samples. Despite exhibiting the best corrosion resistance in the lab furnace testing, the pure Ni suffered from −300 μm metal loss after only 500 h in the in-situ cookstove testing. Conversely, although the 25Ni AFA alloy performed poorly in the lab furnace testing, at 500 h of in-situ cookstove testing, the 25Ni AFA sample showed relatively moderate metal loss of only −62 μm (this sample was not run to longer exposure times).

Cross-Section Microstructures after Corrosion

Fig. 7 shows SEM backscattered electron mode cross-section images of type 310S stainless steel after 500 h of exposure in 600 °C lab furnace, 800 °C lab furnace, and in-situ cookstove testing. Also shown for comparison is a cross-section of a 310S cookstove combustor component (Fig. 7d) from field operation of a cookstove (information on time of operation was not available; the 310S combustor analyzed was not from the same 310S alloy batch used in the other experiments). The corrosion features were quite similar across the lab furnace, in-situ cookstove, and field-used 310S, with loosely adherent external oxide scales tens of microns thick overlying a zone of internal attack.

Elemental mapping by EPMA for 310S after field use, 1000 h in-situ cookstove testing, and 500 h lab furnace testing at 800 °C are shown in Fig. 8. The oxide scales were Fe-rich, with Cr and Si enrichment in the inner oxide scale regions. The internal attack regions were Cr- and Si-rich oxides, with the surrounding metal rich in Ni and depleted in Cr
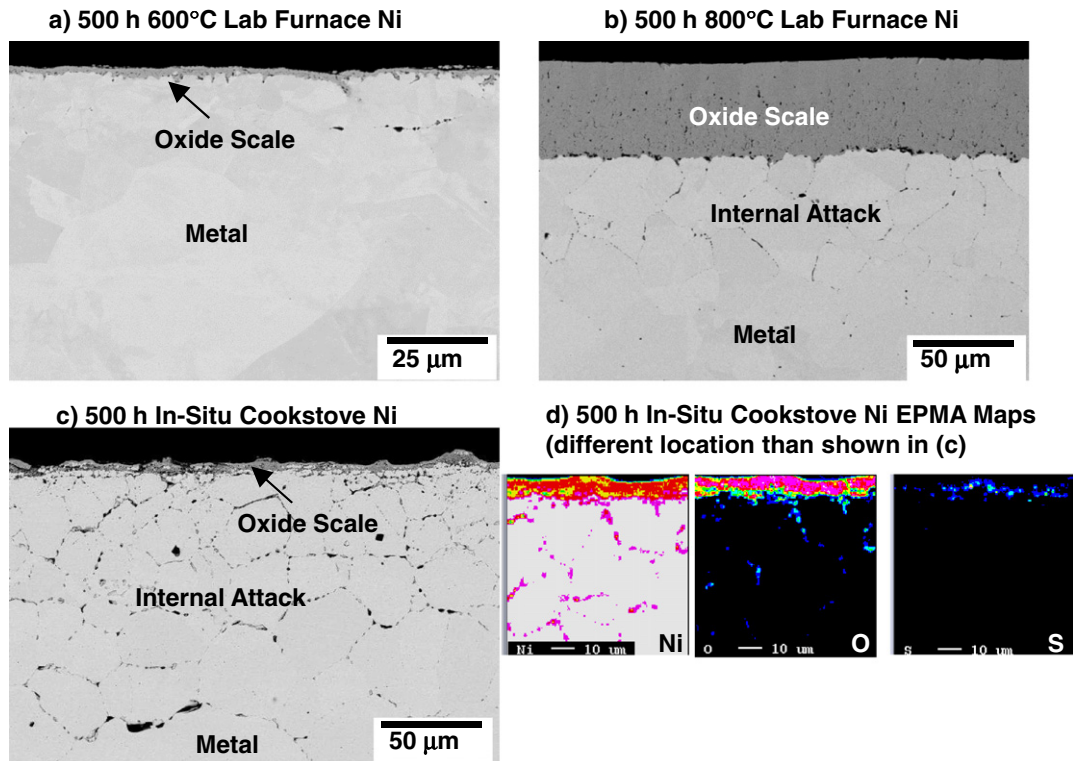

a) 500 h 600°C Lab Furnace Ni

b) 500 h 800°C Lab Furnace Ni

c) 500 h In-Situ Cookstove Ni

d) 500 h In-Situ Cookstove Ni EPMA Maps (different location than shown in (c))

Fig. 9. Cross-section backscattered electron mode SEM images for pure Ni after (a) 500 h, 600 °C lab furnace testing, and (b) after 500 h, 800 °C lab furnace testing. A cross-section backscattered electron mode EPMA image and elemental maps are shown in (c) for pure Ni after 500 h of in-situ cookstove testing.

and Si. For the field-operated and the in-situ cookstove test 310S, S (released by the burning biomass) was also detected in the internal attack zone. Despite the near-absence of S observed in the lab furnace exposure 310S sample, internal attack of Cr and Si was still observed in 310S, which suggests that salt species alone were sufficient to make the alloy susceptible to extensive internal attack. Overall, this comparison indicates that the lab furnace, in-situ cookstove, and the field-operated cookstove all exhibited similar corrosion behavior for type 310S stainless steel, and provides support for the utility of the developed lab furnace and in-situ cookstove test protocols as alloy screening approaches.

Similar Fe-rich oxide scale and internal attack features for lab furnace and in-situ cookstove exposures also were observed for all stainless steel, AFA, and Fe-Cr-X (X = Al, Al + Si) alloys studied, with the notable exception of the pure Ni. (The FeCrSi samples exhibited similar oxide scale structure, but no internal attack in both lab furnace and in-situ cookstove exposures). Fig. 9 shows cross-section images for pure Ni after 500 h 600 °C lab furnace, 800 °C lab furnace, and in-situ cookstove testing. The excellent corrosion resistance in the lab furnace testing resulted from formation of an external Ni-rich oxide scale, with

minor Ni metal grain boundary internal attack evident in the 800 °C exposure and essentially none in the 600 °C exposure. However, extensive internal attack along the Ni metal grain boundaries was observed in the in-situ cookstove testing, which resulted in high metal loss values (Fig. 6). Elemental mapping indicated that the internal attack at the alloy grain boundaries was Ni and O rich. Sulfur was detected near the metal/external scale interface, but not in the internal grain boundary attack zone. Local grain boundary attack areas containing fine Si, C, Fe rich particles were occasionally detected (Si, C, Fe, Mn, Cr, Co, Ca, Mg present as Ni metal impurities, Table 1), but it was not clear if they were definitively associated with the corrosion attack.

Fig. 10 shows a compilation of SEM backscattered electron mode cross-section images for several key alloys after 1000 h of in-situ cookstove testing: commercial stainless steels types 316 L and 446, commercial FeCrAlY, and the developmental model alloys Fe25CrAl, FeCrAlSi, and FeCrSi. The 316 L cross-section (Fig. 10a) was similar to the 310S (Fig. 8b), with an external Fe-rich oxide scale overlying an internal attack zone preferentially along alloy grain boundaries. The depths of the internal attack zones for the 316 L and 310S samples were similar, in the range of ~ − 80 μm, suggesting that the better corrosion
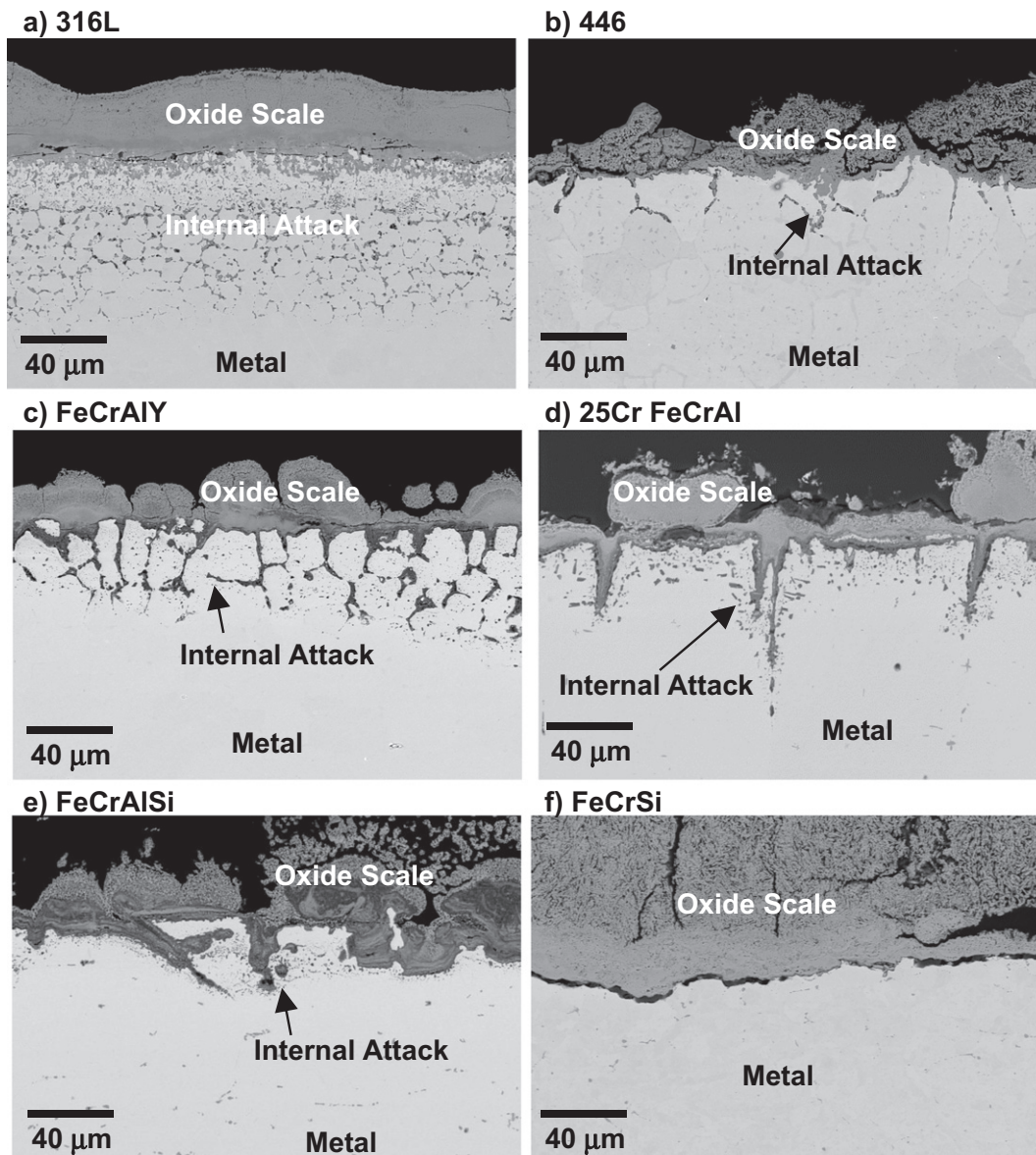

Fig. 10. Cross-section backscattered electron mode SEM images after 1000 h of in-situ cookstove testing for (a) 316 L, (b) 446, (c) FeCrAlY, (d) 25CrFeCrAl, (e) FeCrAlSi, and. (f) FeCrSi.

resistance of 310S (Fig. 6, ~ — 190 μm metal loss for 310S after 1000 h of in-situ cookstove testing vs ~ — 370 μm for 316 L) is due to slower oxide scaling from the higher Cr and Ni levels in type 310S (Table 1). The ferritic 446, FeCrAlY, Fe25CrAl, and FeCrAlSi samples all showed both external scale formation, and internal attack, again primarily along alloy grain boundaries. The extent of internal attack was moderately less than that observed with the austenitic type 310S and 316 L stainless steels, typically in the range of ~ 20–80 μm. In contrast, the FeCrSi sample exhibited external Fe-rich oxide scaling but not internal attack.

The resistance of the FeCrSi alloy to internal attack was the source of its superior corrosion resistance in the 800 °C lab furnace testing (Fig. 5). Low magnification, light microscopy cross-sections of the test sample ends for 310S, FeCrAlY, and FeCrSi after 1000 h of lab furnace testing are shown in Fig. 11. Both the type 310S and FeCrAlY alloys suffered from a transition to extensive internal attack, with the entire sample thickness consumed in some locations. In contrast, no internal attack was observed for the FeCrSi alloy.

Fig. 12 shows backscattered electron mode cross-sections and corresponding EPMA elemental mapping for FeCrAlY after 1000 h of in-situ cookstove testing, FeCrSi after 1000 h of in-situ cookstove testing, and FeCrSi after 500 h of 800 °C lab furnace testing. In the in-situ cookstove testing, the scales formed on both FeCrAlY and FeCrSi were Fe-rich, with fine local porosity associated with Na ingress (Cl also detected in these regions). Chromium and trace Si (Si not shown in maps) were also detected in the external Fe-rich scale formed on FeCrAlY. At the alloy-scale interface in the FeCrAlY (Fig. 12a), locally quasi-continuous regions of Al-rich oxide were observed, overlying an internal attack zone rich in Al-O-S extending inward along alloy grain boundaries (some Si enrichment was also detected in this region). Fine, internal oxidation (and possibly internal nitridation, N not specifically analyzed for) particles associated with Al were also observed between the internally attacked alloy grain boundary regions. The elemental mapping indicated that the alloy in this internal attack region was depleted in Cr and Al relative to the bulk alloy.

For the FeCrSi alloy in both the in-situ cookstove exposure and the 800 °C lab furnace testing, Si was detected in the outer, Fe-rich oxide scales (Fig. 12 b, c). At the alloy/scale interface, both Cr and Si enrichment were also observed. Particularly in the in-situ cookstove test exposure, S enrichment was also detected at the alloy/scale interface. No internal attack was evident in the FeCrSi alloy, although the elemental maps indicated Cr depletion of the alloy beneath the oxide scale, particularly in the 800 °C lab furnace exposure (Fig. 12c).

Discussion

A qualitative ranking of alloys in order from best to worst corrosion resistance based primarily on the cross-section metal loss measurements in conjunction with cross-section microstructure features is provided in Table 3 for each of the 3 test conditions: in-situ cookstove, 600 °C lab furnace, 800 °C lab furnace. The alumina-forming FeCrAl-class alloys exhibited better corrosion resistance than the chromia-forming austenitic 200 and 300 series and ferritic 400 series stainless steels examined under biomass cookstove relevant conditions, although a discrete, thin, and protective alumina-based scale was not formed. Rather, the scales formed by the FeCrAl alloys were still thick and Fe-rich, with enrichment of Al-oxides near the alloy-scale interface, and internal attack of Al beneath the scale (Figs. 10 and 12).

Pre-oxidation of the commercial FeCrAlY alloy to initially form an exclusive alumina surface layer moderately enhanced the high-temperature corrosion resistance of the FeCrAlY, although the benefit was lost (pre-formed alumina scale degraded) with longer exposure times/higher exposure temperatures. These findings are consistent with literature reports that alumina-forming alloys frequently perform better than chromia-forming alloys under biomass-relevant, high-temperature corrosion conditions (Hiramatsu et al., 1989; Spiegel et al., 2003; Israelsson et al., 2015; Li et al., 2007), even when

appreciable corrosion with thick Fe-rich outer oxide scales are encountered. The alumina-forming austenitic (AFA) stainless steels exhibited significantly worse corrosion resistance than did the ferritic FeCrAl-class alloys. The AFA alloys have lower levels of Al and Cr than FeCrAl alloys (Table 1) in order to form an austenitic-based microstructure to achieve good high-temperature creep strength (Brady et al., 2014). A consequence of the lower Al and Cr levels is that AFA falls nearer to the composition borderline for protective alumina scale formation, which makes them more susceptible than FeCrAl to corrosive attack under highly aggressive conditions (Brady et al., 2014).

With the exception of the pure Ni, the relative rankings of the alloys were similar for the lab furnace and in-situ cookstove test methods. This finding suggests that the lab furnace test protocol developed is a useful initial screening method to evaluate candidate alloys for improved biomass cookstove combustors. The in-situ cookstove method is still the preferred alloy evaluation method, with the use of controlled salted wood yielding desired accelerated corrosion conditions (Fig. 3), but is
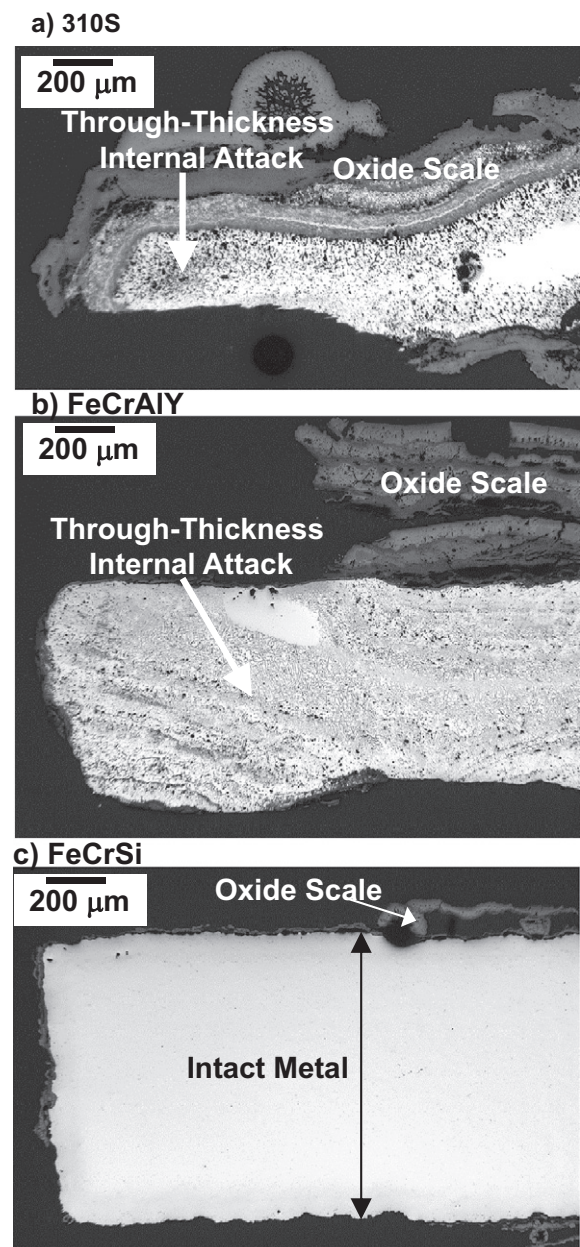

Fig. 11. Cross-section light microscopy images after 1000 h of lab furnace testing at 800 °C for (a) 310S, (b) FeCrAlY, and (c) FeCrSi.
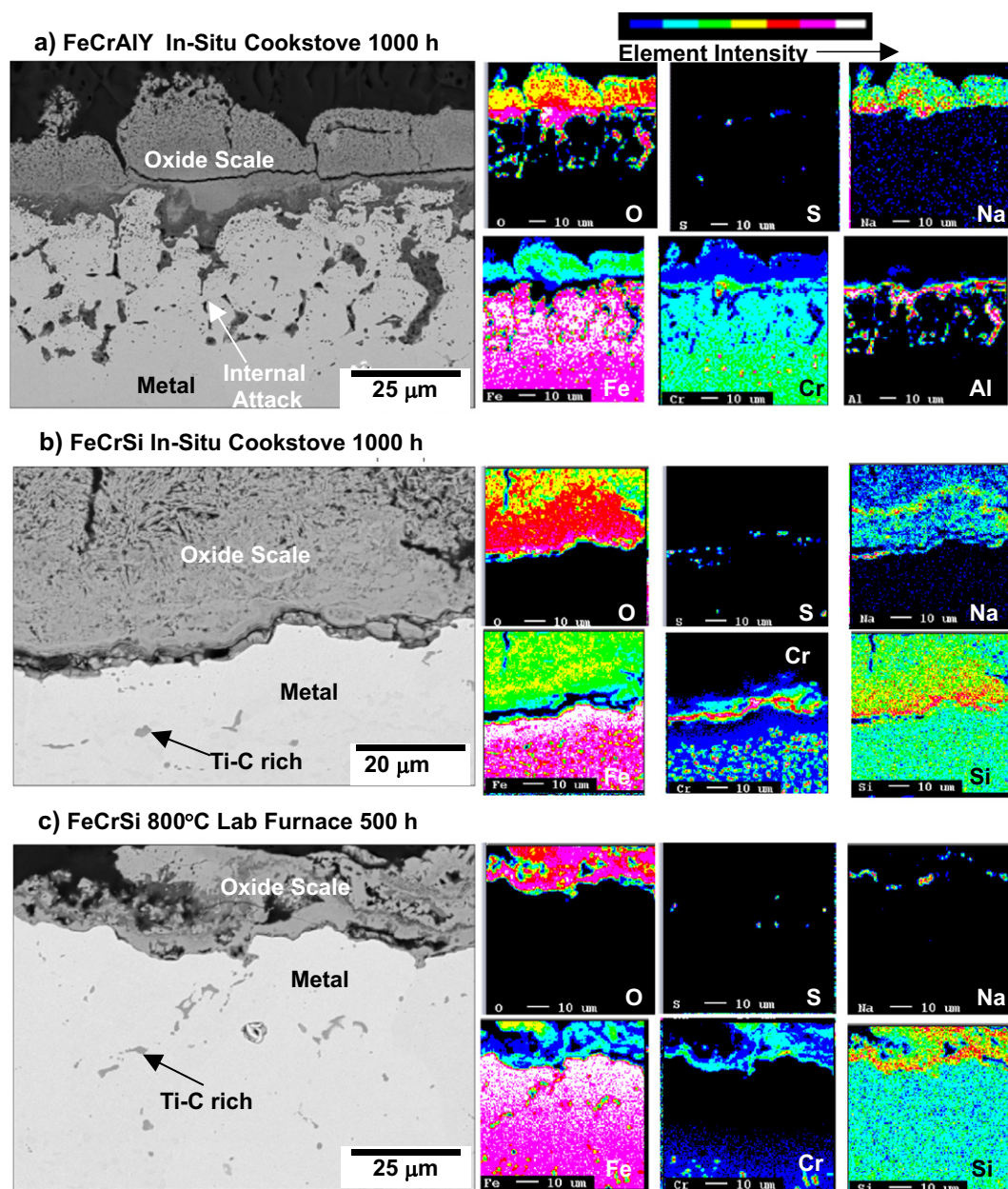
Fig. 12. Cross-section backscattered eelctron mode EPMA images and elemental maps for (a) FeCrAlY after 1000 h of in-situ cookstove testing, (b) FeCrSi after 1000 h of in-situ cookstove testing, and (c) FeCrSi after 500 h of 800 °C lab furnace testing.

also more costly and time consuming to run due to the need to constantly monitor the cookstove and feed it with new wood fuel every ~20 min. The in-situ cookstove testing also yielded similar S ingress characteristics to those observed in field-operated cookstove combustors (Fig. 8), which may play a significant role in the corrosion mechanism for some alloys, particularly if low-melting Ni-S phases are formed, although salt-

species-related attack dominated the alloys studied in the accelerated corrosion conditions of the present work. The extensive metal grain boundary attack (Fig. 9) observed for the pure Ni in the in-situ cookstove exposure (but not the lab furnace testing) did not appear to be the result of S-related attack based on initial EPMA mapping. However, further characterization work is needed to better understand the nature and

Table 3
Qualitative ranking of relative corrosion resistance of alloys in the 3 conditions studied. Most corrosion resistant alloys listed at top, least at bottom. Multiple alloys listed in the same table cell indicate similar levels of corrosion resistance. Note that all of the raw specific mass change and metal loss corrosion data are available in the supplementary material.

In-Situ Cookstove	600 °C Lab Furnace	800 °C Lab Furnace
FeCrAlY, Pre-oxidized FeCrAlY, FeCrAlSi, FeCrSi	Pure Ni, Pre-oxidized FeCrAlY	Pure Ni, FeCrSi
AFA-25Ni, 310S, 446, 25Cr- FeCrAl	FeCrAlY, FeCrAlSi, FeCrSi, 25Cr- FeCrAl	FeCrAlSi
316 L, 201, AFA-20Ni	446, 310S, 316 L	25Cr-FeCrAl, FeCrAlY, Pre-oxidized FeCrAlY,
AFA-12Ni, Pure Ni	AFA-25Ni, AFA-20Ni	316 L, 446, 310S
	201	201, AFA-25Ni, AFA-20Ni, AFA-12Ni
	AFA-12Ni	

mechanism of this internal grain boundary attack, and to identify which species from the biomass (S, C, other?) caused the attack.

The greatest level of corrosion resistance in the present work was exhibited by the developmental FeCrSi alloy (Table 1), particularly in the 800 °C lab furnace testing (Figs. 5, 11, and 12). It has been previously shown that sufficient additions of Si to ferritic Fe-Cr base alloys can beneficially improve high-temperature corrosion resistance in biomass combustion, waste incinerator, and related environments involving high-temperature exposure to salt species (Spiegel et al., 2003; Li et al., 2007, 2004). Model alloys such as Fe-15Cr-5Si wt.% (Spiegel et al., 2003; Li et al., 2007; Grabke et al., 2004) and coatings based on Fe (20–50)Cr- > (3–10)Si wt.% (Grabke et al., 1999) have been reported to exhibit significantly enhanced high-temperature corrosion resistance

a) Fe-15Cr-5Si-0.5Ti-0.08C wt.%

b) Fe-15Cr-3Si-0.5Ti-0.08C wt.%

c) Fe-15Cr-3Si-0.5Ti-0.5C wt.%

Fig. 13. Computational equilibrium thermodynamic predictions for Fe-15Cr-0.5Ti as a function of Si and C content (a-c) using JMatPro_v6 and the Stainless Steel (Fe) database (Sente Software Ltd. Surrey Technology Centre 40 Occam Road GU2 7YG United Kingdom).

in the presence of salt species, beyond that achieved with Al additions. The beneficial effects of Si have been postulated to be related to both increased Cr diffusivity in the alloy to favor formation of a more dense and protective Cr_2O_3 scale (Spiegel et al., 2003; Grabke et al., 2004) and formation of an inner layer rich in SiO_2 at the alloy-scale interface (Li et al., 2007). (SiO_2 does not form at the alloy-scale interface in FeCrAlSi alloys because of the greater thermodynamic stability with oxygen of Al/Al_2O_3 vs Si/SiO_2). Enrichment of Si near the alloy-scale interface was observed for the FeCrSi alloy in the present work (Fig. 12), and both local SiO_2 formation and increased Cr diffusivity effects are consistent with the observed resistance to internal attack by the FeCrSi alloy.

Unfortunately, high levels of Si additions can also result in poor alloy manufacturability, poor mechanical properties, and weldability issues, due in part to the promotion of brittle alpha prime and sigma Cr-rich phases (Bamba et al., 2006; Vanzwieten and Bulloch, 1993; Kim et al., 2015; Hammer et al., 2007). Under some high-temperature oxidation conditions, high levels of Si can also increase the tendency for oxide scale spallation due to the large coefficient of thermal expansion mismatch between SiO_2 and Fe-Cr base alloys (Bamba et al., 2006). Because of this, commercial ferritic stainless steels typically are limited to ~ ≤ 0.5 to 1 wt.% Si. Austenitic stainless steels can generally tolerate higher levels of Si due to their high Ni content which helps resist alpha prime and sigma formation, typically up to ~2 wt.% Si range (Bamba et al., 2006), although some grades as high as 3 to 3.5 wt.% Si are available but used only for niche applications (Hiramatsu et al., 1989). Reports in salt-containing, high-temperature corrosion conditions also indicate a benefit of Si at 3 wt.% and higher in austenitic alloys (Hiramatsu et al., 1989), but not at 1.6 wt.% (Kiamehr et al., 2016). Such high Si austenitics are certainly of interest for improved biomass cookstove combustors, although their relatively high cost due to their Ni content and increased manufacturability challenges from the high Si content are significant drawbacks for the cost of improved biomass cookstoves.

The ferritic FeCrSi alloy of the present work was designed in consideration of the detrimental effects of Si on manufacturability, mechanical properties, and weldability. Computational thermodynamic calculations indicate that, compared to a ferritic Fe-15Cr-5Si base alloy, reduced Si and increased C levels can suppress the predicted formation of brittle sigma and alpha prime phases (Fig. 13). The FeCrSi alloy had an intended nominal composition of Fe-15Cr-3Si-0.5Mn-0.5Ti-0.06C, but was found to be ~Fe-15Cr-2.4Si-0.5Mn-0.5Ti-0.57C on analysis (Table 1). The titanium was added to help limit formation of $M_{23}C_6$ (M = Cr) type precipitates, which can tie up Cr in a manner detrimental to corrosion resistance (sensitization) (Pardo et al., 2007). However, the high C level in the FeCrSi alloy exceeded the level that can be mitigated by the Ti level added, as indicated in the computational thermodynamics which predicted significant $M_{23}C_6$ formation for this alloy (Fig. 13).

Surprisingly, the FeCrSi alloy was readily manufacturable by hot rolling despite the high Si and C content (albeit only evaluated thus far at laboratory scale). The amenability to hot rolling was likely aided by austenite stabilization in the 1100 °C hot-rolling condition employed (Fig. 13 b vs. c), resulting from the high levels of C additions. Further, the FeCrSi alloy also exhibited excellent high-temperature corrosion resistance under biomass-cookstove relevant conditions (Figs. 11, 12). This enhanced corrosion resistance was achieved despite the high levels of C and associated $M_{23}C_6$ formation, and at half the Si level of the literature-reported Fe-15Cr-5Si alloy (Spiegel et al., 2003; Li et al., 2007; Grabke et al., 2004). Additions of 1 wt.% Si in as-cast Fe-14Cr-1Ni-1Si-0.4C have been reported to increase Cr partitioning to the alloy matrix phase and permit ready dissolution of Cr-carbides to support chromia scale formation at 850 °C in pure oxygen (Brady et al., 2000; Durham et al., 1998). A similar effect may have occurred in the FeCrSi alloy of the present work despite the lower (600–800 °C) temperature range.

These findings indicate that ferritic FeCrSi alloy compositions in the range of ~Fe-(13-17Cr)-(2–3.5)Si-(0.2–1)Mn-(0.3–0.7)Ti-(0.1–0.6)C wt.% show promise for use in biomass cookstove combustor components and are of strong interest for further study and scale-up development. Of
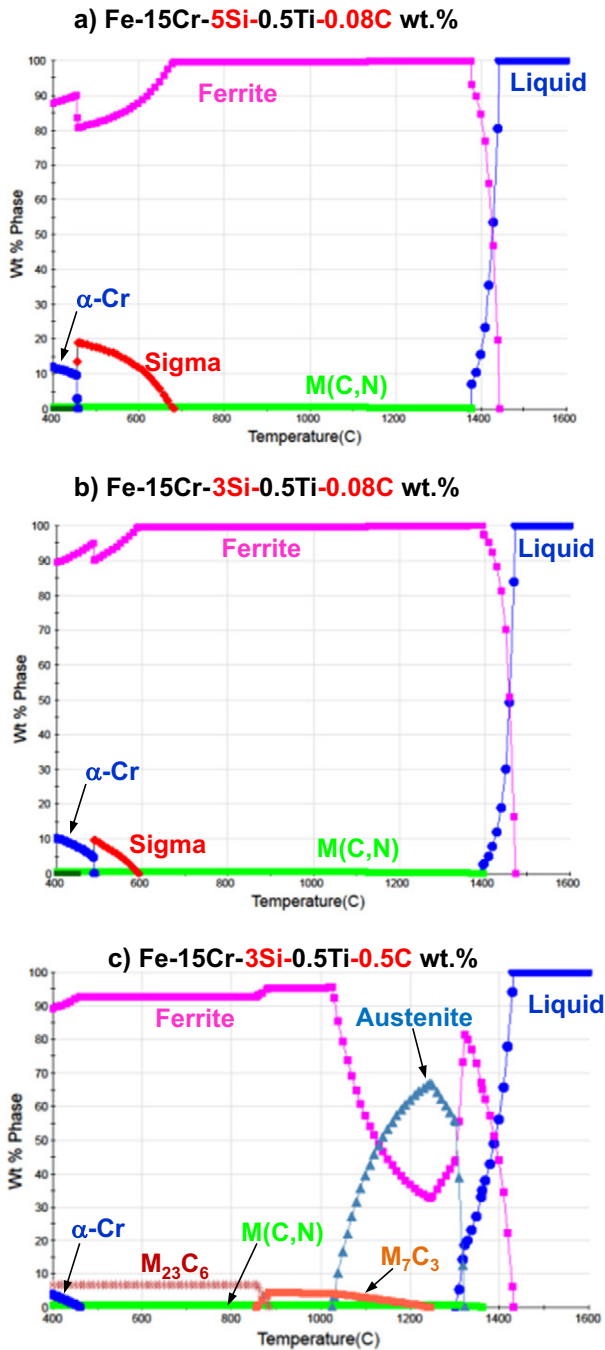
particular relevance to biomass cookstoves, this composition range also has the potential to be less expensive than both FeCrAl alloys and austenitic stainless steels. The higher range of the C levels in the FeCrSi alloys will likely also moderately improve high-temperature strength, which with ferritic alloys is at the borderline for use in improved biomass cookstoves (depending on combustor/cookstove design and operation temperature) (DeFoort et al., 2014). In order to establish commercial viability in cookstoves, future work will need to evaluate both weldability (riveting is also an option in cookstove applications) as well as hot and cold rolling manufacturability under industrial-scale production conditions. Field testing of cookstoves with FeCrSi combustors will also be needed to confirm the beneficial effects on corrosion resistance observed in the lab furnace testing. This Fe-Cr-Si-Mn-Ti-C base alloy composition range may also find use in biomass related power generation applications as alloys and/or coatings. However, it is important to note that the cookstove combustor application has far less stringent requirements for corrosion resistance, mechanical properties, and weldability than do alloys for biomass-fired power generation applications involving industrial scale components, high pressure steam, and operational lifetimes of hundreds of thousands of hours.

Conclusions

1) Accelerated corrosion conditions relevant to biomass cookstove combustors can be achieved by elevated-temperature lab furnace screening test methods using air with water vapor and direct addition of salt to the test sample surfaces, and with in-situ cookstove testing burning control, pre-salted wood.

2) Alumina-forming, ferritic FeCrAl alloys offer superior corrosion resistance under biomass cookstove combustor relevant condition to conventional, chromia-forming ferritic and austenitic stainless steels with Cr contents in the range of ~15–25 wt.% Cr.

3) Ferritic FeCrSi alloys with compositions in the range of ~Fe-(13-17Cr)-(2–3.5)Si-(0.2–1)Mn-(0.3–0.7)Ti-(0.1–0.6)C wt.% show promise for superior corrosion resistance to FeCrAl and conventional, chromia-forming stainless steels under biomass cookstove combustor relevant conditions, at potentially lower cost.

Acknowledgements

Appendix A. Supplementary data

Supplementary data to this article can be found online at http://dx.doi.org/10.1016/j.esd.2016.12.002.

References

Antunes RA, de Oliveira MCL. Corrosion in biomass combustion: A materials selection analysis and its interaction with corrosion mechanisms and mitigation strategies. Corros Sci 2013;76:6–26.

Bamba G, Wouters Y, Galerie A, Charlot F, Dellali A. Thermal oxidation kinetics and oxide scale adhesion of Fe-15Cr alloys as a function of their silicon content. Acta Mater 2006;54:3917–22.

Baxter LL, et al. The behavior of inorganic material in biomass-fired power boilers: field and laboratory experiences. Fuel Process Technol 1998;54:47–78.

Brady MP, Gleeson B, Wright IG. Alloy design strategies for promoting protective oxide scale formation. JOM J Miner Met Mater Soc 2000;52:16–21.

Brady MP, Magee J, Yamamoto Y, Helmick D, Wang L. Co-optimization of wrought alumina-forming austenitic stainless steel composition ranges for high-temperature creep and oxidation/corrosion. Mater Sci Eng A 2014;590:101–15.

DeFoort, M.W., Willson, B.D., Lorenz, N., Brady, M.P., Marchese, A., Miller-Lionberg, D.D. Cookstve Assembly, US Patent 8,899,222 B2 (2014)

Durham RN, Gleeson B, Young DJ. Factors affecting chromium carbide precipitate dissolution during alloy oxidation. Oxid Met 1998;50:139–65.

Ezzati M, Kammen DM. The health impacts of exposure to indoor air pollution from solid fuels in developing countries: Knowledge, gaps, and data needs. Environ Health Perspect 2002;110:1057–68.

Grabke, H.J., Sauthoff, G., Schroer, C., Spiegel, M., Use of steel powder based on Fe-Cr-Si for corrosion resistant coatings, European Patent Application EP 0933443 A1 (1999).

Grabke HJ, Spiegel M, Zahs A. Role of Alloying Elements and Carbides in the Chlorine-Induced Corrosion of Steels and Alloys. Mater Res 2004;7(1):89–95.

Grieshop AP, Marshall JD, Kandlikar M. Health and climate benefits of cookstove replacement options. Energy Policy 2011;39:7530–42.

Hammer JE, et al. The oxidation of ferritic stainless steels in simulated solid-oxide fuel-cell atmospheres. Oxid Met 2007;67:1–38.

Hiramatsu N, Uematsu Y, Tanaka T, Kinugasa M. Effects of Alloying Elements on NaCl-Induced Hot Corrosion Of Stainless-Steels. Mater Sci Eng A 1989;120:319–28.

Israelsson N, Engkvist J, Hellstrom K, Halvarsson M, Svensson JE, Johansson LG. KCl-Induced Corrosion of an FeCrAl Alloy at 600 degrees C in O₂ + H₂O Environment: The Effect of Pre-oxidation. Oxid Met 2015;83(1–2):29–53.

Jonsson T, Slomian A, Lomholt TN, Kiamehr S, Dahl KV. Microstructural investigations of pure nickel exposed to KCl induced high temperature corrosion. Mater High Temp 2015;32:44–9.

Kiamehr S, Dahl KV, Montgomery M, Somers MAJ. KCl-induced high temperature corrosion of selected commercial alloys Part II: alumina and silica-formers. Mater Corros Werkst Korros 2016;67:26–38.

Kim SJ, Kim JK, Park SH. A study on the applicability of Si in low-Mo duplex stainless steel weld metals to improve the corrosion resistance. Scr Mater 2015;96:33–6.

Kshirsagar MP, Kalamkar VR. A comprehensive review on biomass cookstoves and a systematic approach for modern cookstove design. Renew Sustain Energy Rev 2014;30:580–603.

Kumar M, Kumar S, Tyagi SK. Design, development and technological advancement in the biomass cookstoves: A review. Renew Sustain Energy Rev 2013;26:265–85.

Lacey F, Henze D. Global climate impacts of country-level primary carbonaceous aerosol from solid-fuel cookstove emissions. Environ Res Lett 2015;10.

Li YS, Spiegel M, Shimada S. Effect of Al/Si addition on KCl induced corrosion of 9% Cr steel. Mater Lett 2004;58:3787–91.

Li YS, Spiegel M, Shimada S. Corrosion behaviour of various model alloys with NaCl-KCl coating. Mater Chem Phys 2005;93:217–23.

Li YS, Niu Y, Spiegel M. High temperature interaction of Al/Si-modified Fe-Cr alloys with KCl. Corros Sci 2007;49:1799–815.

L'Orange C, DeFoort M, Willson B. Influence of testing parameters on biomass stove performance and development of an improved testing protocol. Energy Sustain Dev 2012;16:3–12.

MacCarty NA, Bryden KM. Modeling of household biomass cookstoves: A review. Energy Sustain Dev 2015;26:1–13.

Okoro SC, Montgomery M, Frandsen FJ, Pantleon K. Effect of Water Vapor on High-Temperature Corrosion under Conditions Mimicking Biomass Firing. Energy Fuel 2015;29:5802–15.

Pardo A, et al. Influence of Ti, C and N concentration on the intergranular corrosion behaviour of AISI 316Ti and 321 stainless steels. Acta Mater 2007;55:2239–51.

Roden CA, Bond TC, Conway S, Benjamin A, Pinel O. Emission factors and real-time optical properties of particles emitted from traditional wood burning cookstoves. Environ Sci Technol 2006;40:6750–7.

Saidur R, Abdelaziz EA, Demirbas A, Hossain MS, Mekhilef S. A review on biomass as a fuel for boilers. Renew Sustain Energy Rev 2011;15:2262–89.

Smith KR, et al. Greenhouse implications of household stoves: An analysis for India. Annu Rev Energy Environ 2000;25:741–63.

Spiegel M, Zahs A, Grabke HJ. Fundamental aspects of chlorine induced corrosion in power plants. Mater High Temp 2003;20:153–9.

Still D, Bentson S, Li HX. Results of Laboratory Testing of 15 Cookstove Designs in Accordance with the ISO/IWA Tiers of Performance. Ecohealth 2015;12:12–24.

Sutar KB, Kohli S, Ravi MR, Ray A. Biomass cookstoves: A review of technical aspects. Renew Sustain Energy Rev 2015;41:1128–66.

Tryner J, Willson BD, Marchese AJ. The effects of fuel type and stove design on emissions and efficiency of natural-draft semi-gasifier biomass cookstoves. Energy Sustain Dev 2014;23:99–109.

Urmee T, Gyamfi S. A review of improved Cookstove technologies and programs. Renew Sustain Energy Rev 2014;33:625–35.

Vanzwieten A, Bulloch JH. Some considerations on the toughness properties of ferritic stainless-steels - a brief review. Int J Press Vessel Pip 1993;56:1–31.

Venkataraman C, Sagar AD, Habib G, Lam N, Smith KR. The Indian National Initiative for Advanced Biomass Cookstoves: The benefits of clean combustion. Energy Sustain Dev 2010;14:63–72.

Wilkinson P, et al. Health and Climate Change 1 Public health benefits of strategies to reduce greenhouse-gas emissions: household energy. Lancet 2009;374:1917–29.

World Health Organization Fact sheet N°292 Household air pollution and health. http://www.who.int/mediacentre/factsheets/fs292/en/, Feb. 2016.

Zhang J, et al. Greenhouse gases and other airborne pollutants from household stoves in China: a database for emission factors. Atmos Environ 2000;34:4537–49.